Author's Accepted Manuscript

Partly standing internal tides in a dendritic submarine canyon observed by an ocean glider

Rob A. Hall, Tahmeena Aslam, Veerle A.I. Huvenne

Cite this article as: Rob A. Hall, Tahmeena Aslam and Veerle A.I. Huvenne, Partly standing internal tides in a dendritic submarine canyon observed by an ocean glider, *Deep-Sea Research Part I* http://dx.doi.org/10.1016/j.dsr.2017.05.015

Partly standing internal tides in a dendritic submarine canyon observed by an ocean glider

Rob A. Hall[a,*], Tahmeena Aslam[a,b], Veerle A. I. Huvenne[c]

[a]*Centre for Ocean and Atmospheric Sciences, School of Environmental Sciences, University of East Anglia, Norwich Research Park, Norwich, NR4 7TJ, UK*
[b]*Centre for Environment Fisheries and Aquaculture Science, Pakefield Road, Lowestoft, Suffolk, NR33 0HT, UK*
[c]*National Oceanography Centre, University of Southampton Waterfront Campus, European Way, Southampton, SO14 3ZH, UK*

Abstract

An autonomous ocean glider is used to make the first direct measurements of internal tides within Whittard Canyon, a large, dendritic submarine canyon system that incises the Celtic Sea continental slope and a site of high benthic biodiversity. This is the first time a glider has been used for targeted observations of internal tides in a submarine canyon. Vertical isopycnal displacement observations at different stations fit a one-dimensional model of partly standing semidiurnal internal tides – comprised of a major, incident wave propagating up the canyon limbs and a minor wave reflected back down-canyon by steep, supercritical bathymetry near the canyon heads. The up-canyon internal tide energy flux in the primary study limb decreases from 9.2 to 2.0 kW m^{-1} over 28 km (a dissipation rate of $1\text{-}2.5 \times 10^{-7}$ W kg^{-1}), comparable to elevated energy fluxes and internal tide driven mixing measured in other canyon systems. Within Whittard Canyon, enhanced mixing is inferred from collapsed temperature-salinity curves and weakened dissolved oxygen concentration gradients near the canyon heads. It has previously been hypothesised that internal tides impact benthic fauna through elevated near-bottom current velocities and particle resuspension. In support of this, we infer order 20 cm s^{-1} near-bottom current velocities in the canyon and observe high concentrations of suspended particulate matter. The glider observations are also used to estimate a 1°C temperature range and 12 µmol kg^{-1} dissolved oxygen concentration range, experienced twice a day by organisms on the canyon walls, due to the presence of internal tides. This study highlights how a well-designed glider mission, incorporating a series of tide-resolving stations at key locations, can be used to understand internal tide dynamics in a region of complex topography, a sampling strategy that is applicable to continental shelves and slopes worldwide.

Keywords: Internal tides, Submarine canyons, Ocean gliders, Celtic Sea, Whittard Canyon

1. Introduction

Submarine canyons are a common geomorphological feature along continental slopes worldwide (Harris and Whiteway, 2011). These dramatic incisions into the continental shelf control exchange of watermasses across the shelf break (Allen and de Madron, 2009), act as conduits for off-shelf transport of organic material and sediment (Kiriakoulakis et al., 2011; Puig et al., 2014), and facilitate burial of organic carbon (Masson et al., 2010) making them an important feature of the global carbon cycle. Their unique ecological characteristics, including steep walls that provide a solid substrate for the development of cold-water coral communities (Huvenne et al., 2011), mean that canyons are often found to be sites of high benthic biodiversity, productivity and biomass (De Leo et al., 2010). As a result, canyons are important commercial fishery sites (Sanchez et al., 2013) and the focus of several marine protected areas (Howell et al., 2010).
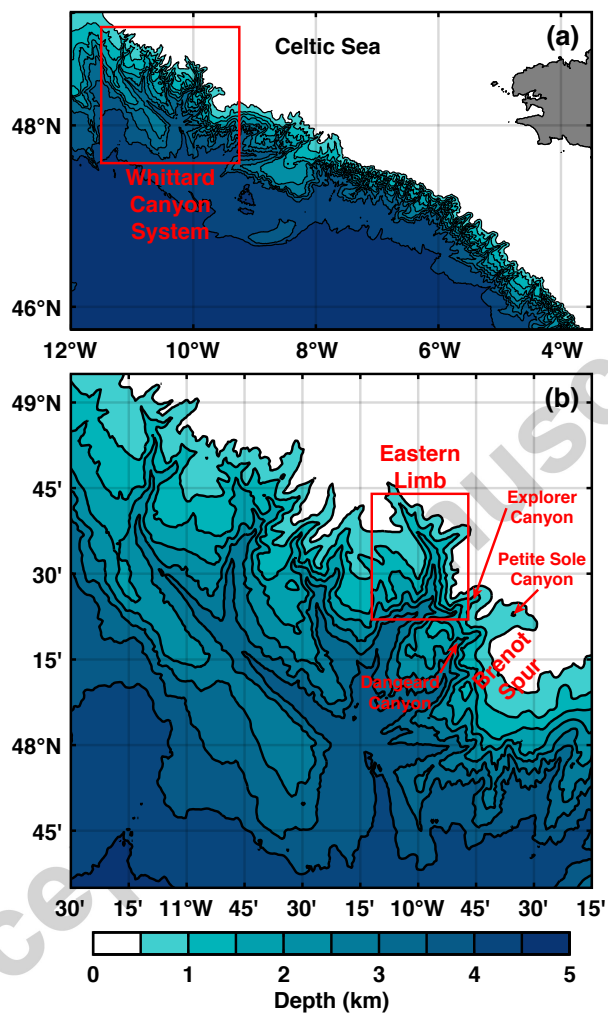

Figure 1: (a) Bathymetry of the Celtic Sea continental slope showing the location of the Whittard Canyon system and (b) the eastern limb (500-m contour interval). The bathymetric dataset is the GEBCO 2014 30 arc-second grid.

2

Observational campaigns in multiple submarine canyons, primary along the North American continental slope, suggest that large-amplitude internal tides are a typical hydrodynamic feature (e.g., Shepard et al., 1974; García Lafuente et al., 1999; Kunze et al., 2002; Waterhouse et al., 2017), with their energy focused towards the canyon floor (Gordon and Marshall, 1976) and head (Hotchkiss and Wunsch, 1982). This topographic focusing of internal tide energy is expected to drive elevated levels of turbulent mixing near canyon heads, a signal observed by Lueck and Osborn (1985), Carter and Gregg (2002) and Kunze et al. (2012) in Monterey Canyon and by Lee et al. (2009) in Gaoping Canyon. Typically, internal tides are observed to propagate up-canyon, from deep water onto the shelf, but observational and modelling studies (Petruncio et al., 1998; Zhao et al., 2012; Hall et al., 2014) have shown that the internal tide in Monterey Canyon is sometimes a partly standing wave – comprised of a major wave propagating up-canyon and a minor wave reflected back down-canyon by steep bathymetry near the canyon head. Recent observations have shown that the semidiurnal internal tide in Eel Canyon is also a partly standing wave (Waterhouse et al., 2017). The distinction between fully propagating (progressive) waves and partly standing waves is important because the up-canyon energy flux of a partly standing wave is less than that of a progressive wave with the same forcing amplitude (Martini et al., 2007). This implies less energy dissipation in the canyon and so an overestimation of internal tide driven mixing.

The majority of well-studied submarine canyons are simple linear incisions (e.g., Hydrographers, Ascension and Congo Canyons) or have meandering morphology (e.g., Monterey, Gaoping and Nazaré Canyons). Branching (dendritic) canyons have received far less attention despite the fact that this morphological type is common worldwide and specifically around the Mediterranean (Harris and Whiteway, 2011). Here, we use an autonomous ocean glider to make the first direct measurements of internal tides within Whittard Canyon, a large, dendritic submarine canyon system that incises the Celtic Sea continental slope (Fig. 1). Despite being been widely studied for sedimentological and biological processes (see Amaro et al., 2016, for a review) the physical oceanography of the canyon has received only limited attention (Johnson et al., 2013; Wilson et al., 2015; Porter et al., 2016). Internal tides and turbulent mixing processes in the wider Celtic Sea and Bay of Biscay region have been previously investigated (e.g., New, 1988; Green et al., 2008; Sharples et al., 2009; Hopkins et al., 2014), but it is clear from high-resolution numerical modelling studies (Vlasenko et al., 2014; Vlasenko and Stashchuk, 2015) that the internal tide field is highly heterogeneous, three-dimensional, and shaped by local bathymetry. Specifically, three-dimensional focusing of internal tide energy within Petite Sole Canyon (part of the wider Whittard Canyon system) has been observed and modelled by Vlasenko et al. (2016). A broad understanding of internal tide dynamics within Whittard Canyon will help the extrapolation of results along the highly corrugated Celtic Sea continental slope and to dendritic canyons worldwide.

Ocean gliders have previously been used to make observations of internal tides in the Luzon Strait (see Rudnick, 2016, for a review), Californian continental slope (Johnston and Rudnick, 2015) and Tasman Sea (Johnston et al., 2015), but this is the first time a glider has been used for targeted observations of internal tides in a submarine canyon. Gliders provide an alternative view of the internal tide field to ship CTD surveys or fixed mooring timeseries. Large gradients in internal tide energy, typical of submarine canyons, can be mapped at higher spatial resolution than possible with a limited number of moorings, while their autonomous nature and long endurance allow a larger number of tide-resolving stations to be occupied than during a typical CTD survey. In Section 2, the glider observations and internal tide analysis methods are described. In Section 3, partly standing internal tides are diagnosed and a canyon energy budget constructed. Enhanced mixing within the canyon is inferred in Section 4. The results are discussed in Section 5 and potential impact of the observed internal tides on benthic fauna assessed. Key results of the study are summarised in Section 6.

2. Glider observations

An iRobot 1KA Seaglider (SG537; Eriksen et al., 2001) was deployed over the eastern limb of Whittard Canyon for 22 days between 15th August and 6th September 2015. During this time it occupied 8 virtual mooring (VM) stations with two stations occupied twice, approximately at spring and neap tide (Fig. 2a,b).
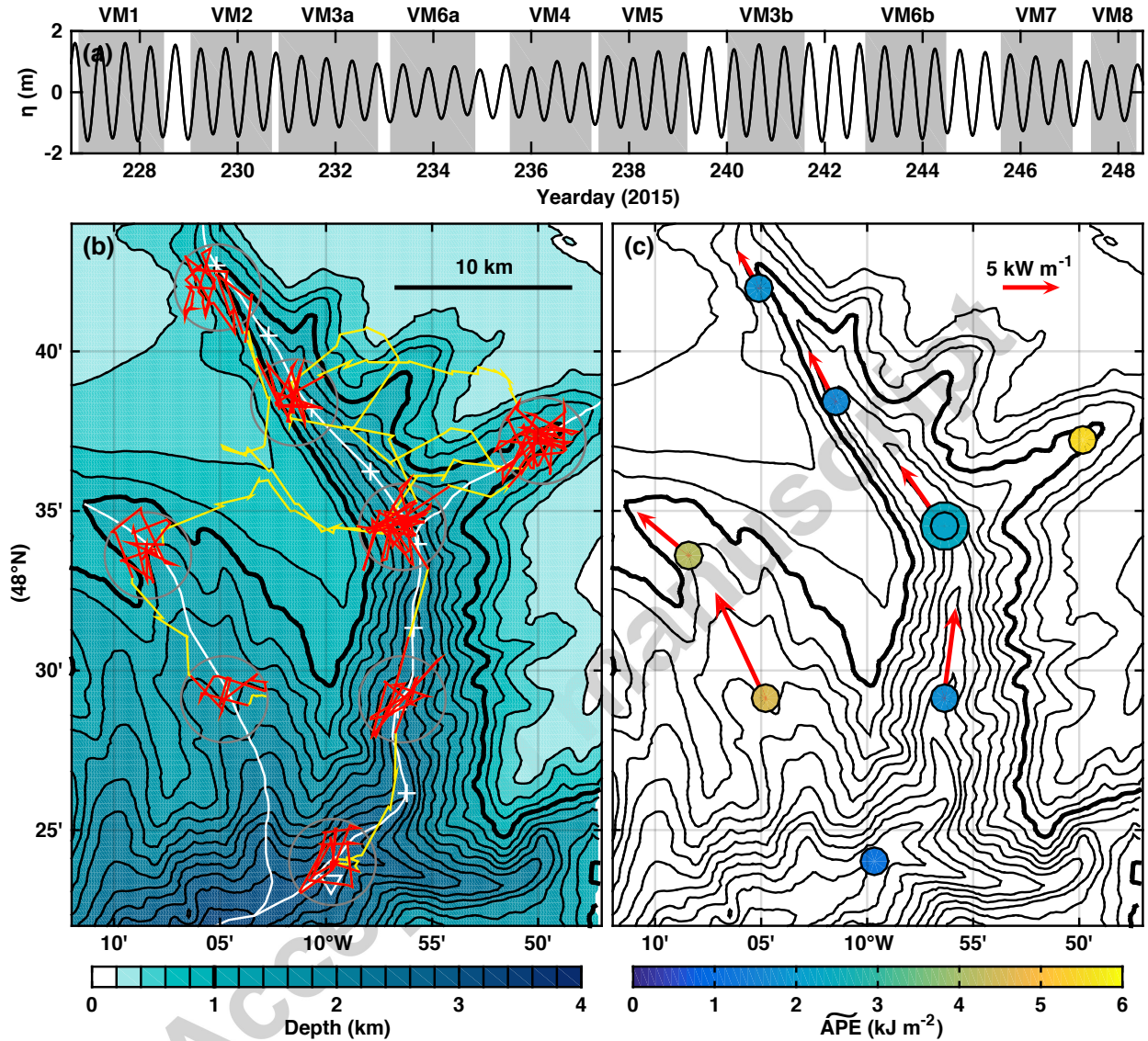
Figure 2: (a) TPXO surface elevation (M_2, K_1 and S_2 tidal constituents) showing the timing of the glider stations relative to the spring-neap cycle. (b) Bathymetry of the eastern limb of Whittard Canyon (INFOMAR, 200-m contour interval) and the glider's path: red is where it occupied a station; yellow is where it transited between stations. 5-km diameter 'watch circles' are indicated in grey. The white lines are the canyon limb thalwegs. The white triangle is the location of the ship CTD cast. (c) M_2 available potential energy at each station, vertically integrated from the surface to 1000 m ($\widetilde{\mathrm{APE}}$). The red arrows are depth-integrated M_2 internal tide energy flux vectors (F_x^{obs}) where the 1-D internal tide model has been successfully applied.

Table 1: Number of dives, total time in hours, and data scatter statistics (mean, standard deviation and percent less than 2.5 km) for each station occupation. ΔX is distance in kilometres from each glider sample to the target location. λ is theoretical M_2 mode-1 horizontal wavelength in kilometres. Also shown is the spring-neap modulation (m_{sn}), applied to $\xi_A^{M_2}$ in order to remove the influence of the S_2 internal tide, along with maximum displacement amplitude and $\widetilde{\text{APE}}$, both with and without modulation ($\xi_A^{M_2}$ and ξ_A are in metres, $\widetilde{\text{APE}}$ is in kJ m^{-2}). The two occupations of VM3 are in bold. The results for VM6b are omitted because the internal tide was inadequately resolved.

VM	Dives	Time	Data scatter			λ	m_{sn}	Unmodulated		Modulated	
			ΔX_{mean}	ΔX_{std}	$\Delta X < 2.5$ km			$\xi_A^{M_2}$	$\widetilde{\text{APE}}$	ξ_A	$\widetilde{\text{APE}}$
1	15	42.0	1.10	0.56	99.9%	120	1.33	58	2.0	44	1.2
2	14	39.9	1.25	0.73	93.2%	110	1.16	71	2.3	61	1.7
3a	**17**	**48.8**	**1.03**	**0.63**	**96.4%**	**95**	**0.89**	**46**	**1.7**	**52**	**2.2**
6a	16	41.8	1.04	0.67	96.3%	60	0.68	76	2.5	111	5.5
4	14	40.1	0.96	0.61	97.3%	85	0.74	42	0.9	56	1.6
5	22	43.6	1.52	0.67	92.7%	60	0.98	53	1.4	54	1.8
3b	**14**	**37.9**	**1.21**	**0.69**	**94.7%**	**95**	**1.28**	**79**	**3.8**	**62**	**2.4**
6b	15	39.7	1.40	0.70	92.0%	60					
7	13	35.3	1.11	0.66	97.6%	70	0.93	80	3.5	87	4.1
8	9	22.3	1.04	0.63	98.8%	90	0.74	55	2.4	74	4.6
Total	149	391.3	1.17	0.68	95.7%						

Each station occupation was at least 35 hours with the glider completing 13-22 dives[1] to 1000 m or the seabed (whichever was shallower). The average time to complete a full 1000-m dive cycle was 2 hours 50 minutes. Data were collected during both the descending and ascending sections of each dive, yielding 26-44 profiles over 35-48 hours for each station occupation. This is adequate to resolve the M_2 internal tide (Nash et al., 2005). Glider location at the surface, before and after each dive, was given by GPS position. Subsurface sample locations were approximated by linearly interpolating surface latitude and longitude onto sample time. When occupying a station, 95% of glider samples were within 2.5 km of the target location (Fig. 2b; Table 1) and so data scatter was small compared to theoretical M_2 mode-1 horizontal wavelength for the study region (60-120 km). Glider data were therefore considered fixed-point timeseries when occupying stations.

The glider was equipped with a standard Sea-Bird Electronics conductivity-temperature (CT) sail sampling at 0.2 Hz and the data processed using the UEA Seaglider Toolbox (https://bitbucket.org/bastienqueste/uea-seaglider-toobox) following Queste (2014). Conductivity data were corrected for thermal hysteresis following Garau et al. (2011) and the Seaglider flight model regressed using a method adapted from Frajka-Williams et al. (2011). As the CT sail was unpumped, samples were flagged when glider's vertical velocity was less than 5 cm s^{-1}. Temperature-salinity profiles from descents and ascents were independently averaged (median value) in 5-m depth bins, typically with 3-5 samples per bin. Sample time was averaged into the same bins to allow accurate temporal analysis at all depths. Absolute salinity (S_A), conservative temperature (Θ) and potential density (ρ) in each bin were calculated using the TEOS-10 equation of state (IOC et al., 2010). In addition to the CT sail, the glider was equipped with an Aanderaa 4330F dissolved oxygen optode and a WETLabs Eco Puck optical sensor measuring chlorophyll a fluorescence at 470/695 nm and scattering at 470 nm (blue) and 700 nm (red) wavelengths. Both additional sensors sampled every 30 seconds.

2.1. Internal tide analysis

For each station occupation, the time-average potential density profile, $\overline{\rho}(z)$, was calculated then vertical isopycnal displacement, $\xi(z,t) = -\rho'(\partial \overline{\rho}/\partial z)^{-1}$, calculated from density anomaly, $\rho'(z,t) = \rho(z,t) - \overline{\rho}(z)$.

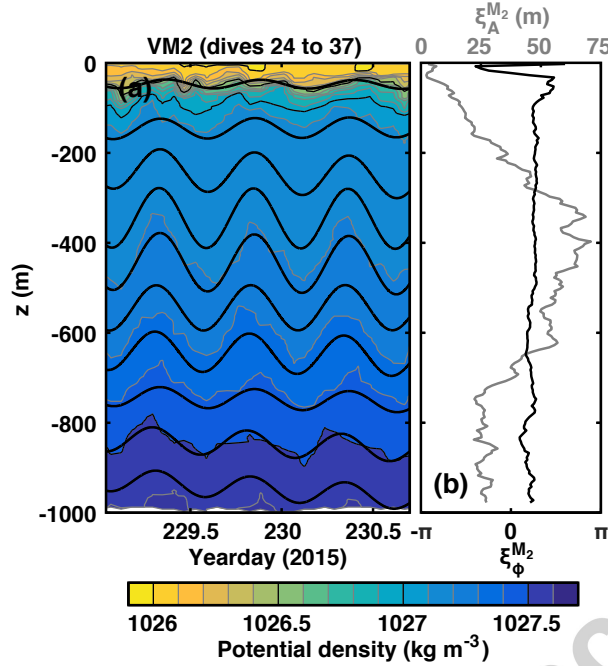[1]Only 9 dives over 22 hours were completed at VM8.

Figure 3: (a) 40-hour timeseries of potential density at VM2 overlaid with M_2 harmonically filtered vertical isopycnal displacement every 100 m (black lines). The dotted white line is the glider's path and shows the temporal sampling resolution. (b) Amplitude and phase of M_2 displacement from the harmonic analyses.

An M_2 harmonic analysis was applied to isopycnal displacement on each depth level, yielding profiles of M_2 displacement amplitudes ($\xi_A^{M_2}$) and phases ($\xi_\phi^{M_2}$). As an example, harmonically filtered isopycnal displacement at VM2 is shown in Figure 3a (black lines); the corresponding profiles of $\xi_A^{M_2}$ and $\xi_\phi^{M_2}$ are shown in Figure 3b. This example was chosen because it features both large displacement amplitudes and particularly uniform displacement phase.

The station timeseries were too short to separately resolve the S_2 internal tide, so the spring-neap cycle was removed by assuming a local generation site and therefore that the internal spring-neap cycle was phase-locked and proportional to the surface spring-neap cycle. Using the TPXO inverse model European Shelf solution (Egbert and Erofeeva, 2002; Egbert et al., 2010, http://volkov.oce.orst.edu/tides/) to define study region-average surface elevation amplitudes for the M_2 and S_2 tides ($\eta_A^{M_2}$ and $\eta_A^{S_2}$), the spring-neap modulation of surface elevation was modelled

$$m_{sn}(t) = 1 + \frac{\eta_A^{S_2}}{\eta_A^{M_2}} \cos(\omega_{sn} t - \phi_{sn}) \tag{1}$$

and defined for the mid-point time of each station occupation. $\omega_{sn} = 4.93 \times 10^{-6}$ s^{-1} is the spring-neap frequency and ϕ_{sn} is the spring-neap phase determined from TPXO. This modulation (Table 1) was applied to the observed profiles of M_2 displacement amplitude in order to remove the influence of the S_2 internal tide ($\xi_A = \xi_A^{M_2}/m_{sn}$). M_2 displacement phase was not affected by the modulation so $\xi_\phi = \xi_\phi^{M_2}$.

Isopycnal displacement amplitudes up to 80 m were directly observed (VM7; Table 1); increased to 87 m by the modulation. However, the largest modulated displacement amplitude was at VM6a (111 m), due to it being occupied close to neap tide. At each station ξ_A and ξ_ϕ display variability with depth (e.g., Fig. 4b), but there is coherence between each analysed depth level. A notable exception is VM3, located at a canyon branch, where for both occupations there is a phase discontinuity at 700 m associated with a decrease in amplitude to near-zero. As this coincides with the depth of the western canyon rim, the discontinuity is

6

possibly due to a change in internal tide generation site. Below 700 m the internal tide can only be influenced by generation sites to the south, whereas above 700 m sites to the west can also be an influence.

To characterise ξ_ϕ as a depth-invariant metric for later comparison with a one-dimensional model, we calculate the mean value of $\xi_\phi(z)$, linearly weighted by $\xi_A(z)$, for each station occupation $(\widetilde{\xi_\phi})$.

2.2. Available potential energy

For each station occupation, profiles of M_2 available potential energy were calculated and vertically integrated from the surface to 1000 m,

$$\widetilde{\mathrm{APE}} = \frac{1}{4}\rho_0 \int_{-1000}^{0} N^2 \xi_A^2 \, dz, \tag{2}$$

where $\rho_0 = 1028$ kg m^{-3} is a reference density, $N = \sqrt{-g/\rho_0(\partial\overline{\rho}/\partial z)}$ is the buoyancy frequency, and g is the acceleration due to gravity.

The spatial distribution of $\widetilde{\mathrm{APE}}$ is shown in Figure 2c. Similar values for the two occupations of VM3 (2.24 and 2.37 kJ m^{-2}; Table 1) are evidence that the spring-neap correction was successful and that the underlying assumptions are reasonable. The two occupations of VM6 cannot be compared because the second occupation failed to adequately resolve the internal tide. The potential density timeseries from VM6b (not shown) suggests the internal tide had a bore-like structure that was inadequately resolved by the order 3-hour glider sampling at the seabed. This type of nonlinear waveform has been observed in other submarine canyons (e.g., Monterey Canyon; Key, 1999) and is a plausible explanation given the timing of the occupation, just after spring tide.

3. Partly standing internal tides

To determine the type of internal tide present in the canyon, partly standing internal wave theory developed by Petruncio et al. (1998), Nash et al. (2004, 2006) and Martini et al. (2007) is used to generate a one-dimensional zonal partly standing internal tide model with realistic canyon stratification and bathymetry. The distributions of $\widetilde{\xi_\phi}$ and $\widetilde{\mathrm{APE}}$ along the main eastern limb (VMs 2, 3a, 4, and 5) are then used to constrain the amplitudes and phases of the major and minor component waves.

Following Martini et al. (2007), two converging mode-1 internal waves of unequal amplitude and phase in depth-varying but horizontally uniform stratification can be described by

$$u(x, z, t) = [u_0 \sin(k_x x - \omega t - \phi_0) - u_1 \sin(k_x x + \omega t - \phi_1)]A(z), \tag{3}$$

$$v(x, z, t) = [-u_0 \cos(k_x x - \omega t - \phi_0) - u_1 \cos(k_x x + \omega t - \phi_1)]A(z)\frac{f}{\omega}, \text{ and} \tag{4}$$

$$\xi(x, z, t) = [u_0 \sin(k_x x - \omega t - \phi_0) + u_1 \sin(k_x x + \omega t - \phi_1)]B(z)\frac{1}{\omega}\left(\frac{\omega^2 - f^2}{N^2(z) - \omega^2}\right)^{1/2}, \tag{5}$$

where u_0 and u_1 are the velocity amplitudes of the eastward and westward propagating waves, respectively, ϕ_0 and ϕ_1 are the eastward and westward wave phases, ω is the wave frequency, and f is the inertial frequency. $A(z)$ and $B(z)$ are the mode-1 profiles of horizontal velocity and vertical displacement, respectively, calculated by solving the boundary value problem for a given $N(z)$ (Gill, 1982). Mode-1 eigenspeed (c_n) is used to determine mode-1 horizontal wavenumber, $k_x = \sqrt{\omega^2 - f^2}/c_n$ (Gill, 1982). Unlike the flat bottom case modelled by Martini et al. (2007), the depth of a typical submarine canyon decreases towards its head. In this sloping bottom case, A and B become functions of both x and z, and c_n decreases in the up-slope direction. To account for the resulting up-slope increase in k_x, the spatial component of wave phase is defined $k_x x = \int_0^x k_x \, dx$.

We model four possible M_2 mode-1 internal tide fields for the main eastern limb of Whittard Canyon. Each has identical eastward (up-canyon) wave velocity amplitudes ($u_0 = 0.16$ m s^{-1}), but westward (down-canyon) wave velocity amplitude is defined as a percentage of u_0: 0% is a fully progressive wave; 100% is
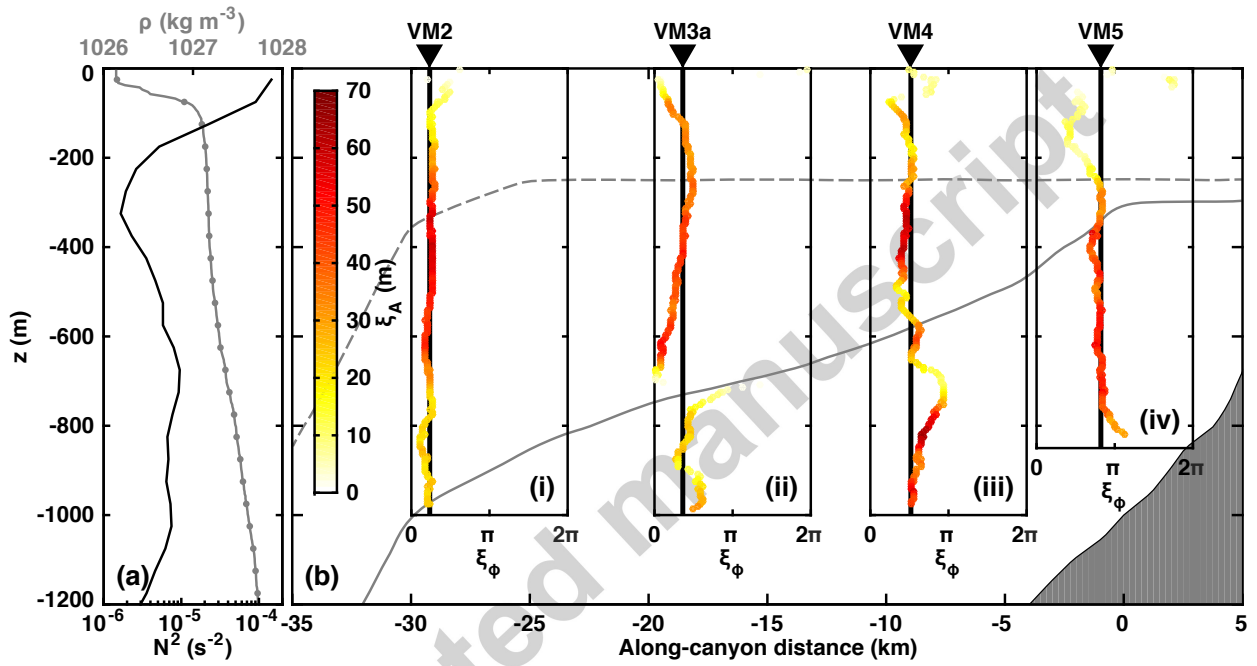
Figure 4: (a) Profile of potential density from the ship CTD cast (interpolated onto 50-m depth levels) and buoyancy frequency squared on the same depth levels. (b) M_2 vertical isopycnal displacement phase at four stations along the main canyon limb (subpanels i to iv) with displacement amplitude indicated by colour. In each subpanel the thick black line indicates displacement phase for a 25% partly standing M_2 mode-1 internal tide propagating up-canyon. The solid (dashed) grey line is the depth of the western (eastern) canyon rim.

a fully standing wave; 25% and 50% are partly standing waves. For all models $\phi_0 = 75°$ and $\phi_1 = 190°$. The domain is 40 km long with realistic along-canyon depth (H) derived from 250-m resolution bathymetry provided by the Geological Survey of Ireland INFOMAR programme (http://www.infomar.ie). H decreases from 2578 m to 678 m in the x-direction, an overall slope gradient of 0.0475. $A(x, z)$, $B(x, z)$ and $c_n(x)$ are calculated every 250 m in the horizontal using $N(z)$ from a 2900 m deep ship CTD cast near VM1, completed just after the glider deployment, interpolated onto 50-m depth levels (Fig. 4a). For comparison with the observations, $\xi(x, z, t)$ is decomposed into $\xi_A(x, z)$ and $\xi_\phi(x, z)$. ξ_ϕ is depth-invariant for mode-1 waves, so can be directly compared with $\widetilde{\xi_\phi}$.

All four models feature a nonlinear gradient of ξ_ϕ, an effect of the sloping bottom, but the curvature increases as percentage standing wave increases (Fig. 5a). For the fully standing wave case **u**-nodes and ξ-nodes exist (where **u** and ξ, respectively, go to zero); ξ_ϕ is uniform and 180° out of phase between consecutive ξ-nodes. The magnitude of the along-canyon oscillation of $\widetilde{\text{APE}}$ increases as percentage standing wave increases (Fig. 5b). As expected, $\widetilde{\text{APE}}$ is minimum at the ξ-node for partly standing waves and goes to zero at the same location for the fully standing wave case. Maximum $\widetilde{\text{APE}}$ is slightly up-canyon of the **u**-node.

The model that best fits the observations of $\widetilde{\xi_\phi}$ and $\widetilde{\text{APE}}$ is the 25% partly standing internal tide. The values of u_0, ϕ_0 and ϕ_1 are tuned to best fit the observations, but only a 25% partly standing wave features the correct along-canyon gradient of ξ_ϕ (Fig. 5a). Model $\widetilde{\text{APE}}$ is also a good fit to the observations at three of the four stations, only at VM5 is $\widetilde{\text{APE}}$ notably underestimated (Fig. 5b). In addition, the prescribed velocity amplitudes yield a range of maximum displacement amplitudes (42-69 m) similar to observed (Table 1). Recalculating observed $\widetilde{\text{APE}}$ using unmodulated displacement amplitudes (i.e., including the internal spring-neap cycle) results in an along-canyon distribution that cannot be recreated by any of the models (Fig. 5b, empty circles).

The model underestimation of $\widetilde{\text{APE}}$ near the head of the main canyon limb is possibly because the internal tide field at VM5 was the least well-resolved. Due to the narrowness of the canyon, only 8 of the 22 dives went deeper than 800 m. Robust M_2 harmonic analyses were only possible down to 820 m, despite the canyon floor being ≈1050 m deep at this location. To account for this difference in the depth of observations, $\widetilde{\text{APE}}$ was scaled to 1000 m at all stations. This has a negligible effect on the other VMs (where robust harmonic analyses were possible down to at least 965 m), but may under or overestimate $\widetilde{\text{APE}}$ at VM5 depending on whether near-bottom energy flux was greater or less than the depth average. Another possible explanation of the underestimation of $\widetilde{\text{APE}}$ near the head of the canyon is that the 1-D model cannot account for the narrowing of the canyon and lateral focusing of internal tide energy.

3.1. Canyon energy budget

Assuming a 25% partly standing M_2 mode-1 internal tide propagating up-canyon, we construct a 1-D energy budget for the main canyon limb (Fig. 5c). Depth-integrated available potential energy is calculated

$$\text{APE} = \frac{1}{2}\rho_0 \int_{-H}^{0} N^2 \langle \xi^2 \rangle \, dz, \tag{6}$$

where $\langle \cdot \rangle$ denotes an average over a tidal cycle. Depth-integrated horizontal kinetic energy is calculated

$$\text{HKE} = \frac{1}{2}\rho_0 \int_{-H}^{0} \langle u^2 + v^2 \rangle \, dz. \tag{7}$$

Following Kunze et al. (2002) and Nash et al. (2005), depth-integrated internal tide energy flux is calculated

$$\mathbf{F} = \int_{-H}^{0} \langle \mathbf{u}p' \rangle \, dz, \tag{8}$$

where p' is pressure perturbation, calculated by integrating the hydrostatic equation from the surface, $p' = p'_{\text{surf}} + \rho_0 \int_{z}^{0} N^2 \xi \, dz$. Pressure perturbation at the surface due to the internal tide (p'_{surf}) is determined by applying the baroclinicity condition for pressure, $\int_{-H}^{0} p' \, dz = 0$.
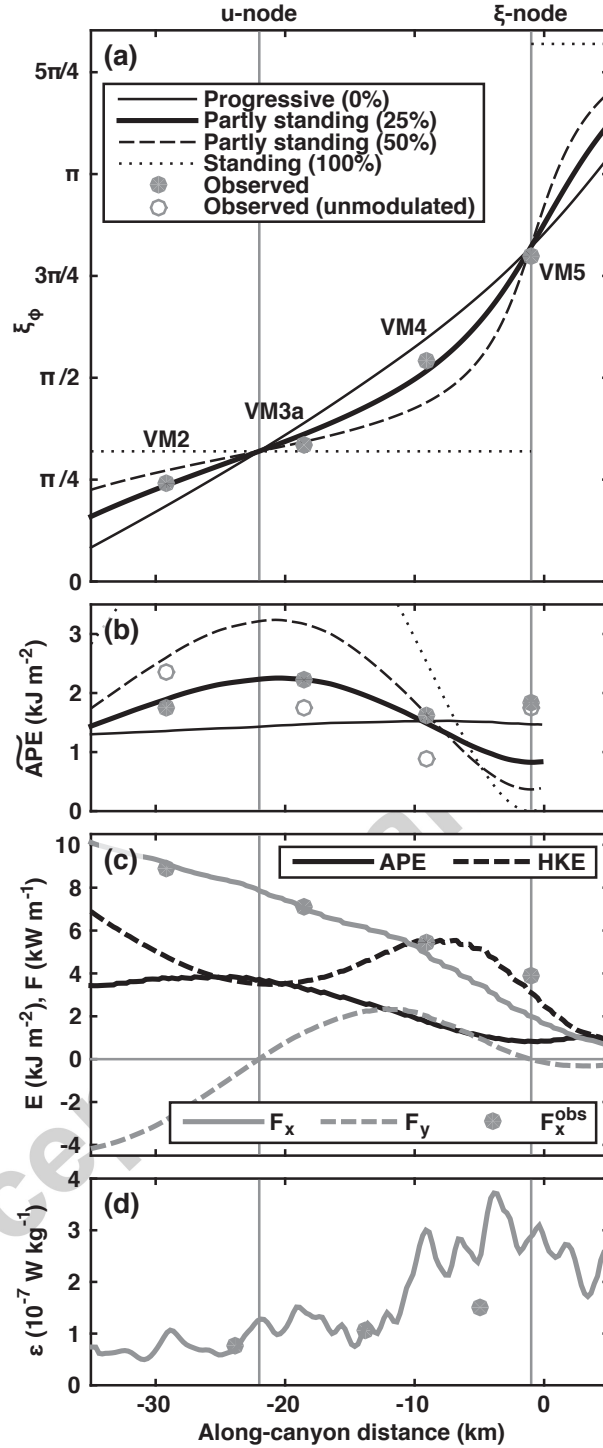
Figure 5: (a) Vertical isopycnal displacement phase with distance along the main canyon limb for progressive, partly standing and standing M_2 mode-1 internal tides compared with observed displacement phase $(\widetilde{\xi_\phi})$. **u**-nodes and ξ-nodes for the fully standing wave case are indicated by grey lines. (b) $\widetilde{\mathrm{APE}}$ for the same internal tides as (a) compared with observed $\widetilde{\mathrm{APE}}$ with and without modulation. (c) APE, HKE, and along-canyon (F_x) and across-canyon (F_y) energy fluxes for the 25% partly standing wave case compared with along-canyon energy flux calculated using observed available potential energy (F_x^{obs}). (d) Internal tide dissipation rate (ε) calculated from the convergence of F_x (thick grey line) and F_x^{obs} (grey circles).

10

As with the flat bottom case shown by Martini et al. (2007), both APE and HKE oscillate along-canyon[2] at twice the spatial frequency of the component waves, but the oscillations shorten towards the canyon head as k_x increases and are superposed on a trend of decreasing total energy density (E = HKE + APE). As expected, local HKE and APE minima are found near the **u**-nodes and ξ-nodes, respectively. A local HKE maximum is found at -8 km while a APE maximum is found at -24 km. Depth-integrated across-canyon energy flux (F_y) also oscillates at twice the spatial frequency of the component waves, zero at the **u**- and ξ-nodes, positive between -1 km and -22 km, and negative farther up- and down-canyon. Given the approximately south-to-north orientation of the actual canyon, positive (negative) across-canyon energy flux corresponds to westward (eastward). Depth-integrated along-canyon energy flux (F_x) is up-canyon and decreases monotonically from 9.2 kW m^{-1} at VM2 to 2.0 kW m^{-1} at VM5, a distance of 28 km. Finally, internal tide dissipation rate can be calculated $\varepsilon = -\nabla F_x/(\rho_0 H)$ and increases from 1×10^{-7} W kg^{-1} down-canyon of -10 km to 2.5×10^{-7} W kg^{-1} up-canyon of -10 km (Fig. 5d).

An alternative estimate of F_x at the station locations can be arrived at by first calculating the model HKE/APE ratio (E_{ratio}) and perceived group speed, $c_g = F_x/E$ (Alford and Zhao, 2007), then recalculating $F_x^{obs} = c_g \text{APE}(E_{ratio}+1)$ using observed available potential energy over the depth range of observations and model available potential energy beneath. F_x^{obs} only notably deviates from F_x at VM5 where it is increased to 3.9 kW m^{-1}. Using F_x^{obs}, the dissipation rate between VM4 and VM5 is decreased to 1.5×10^{-7} W kg^{-1}.

4. Mixing proxies

No direct measurements of turbulent mixing were made during the study, however, enhanced mixing within the eastern limb of Whittard Canyon is inferred from two sources. Firstly, temperature-salinity plots for the four stations along the main canyon limb (VMs 2-5) show a progressive collapse onto a mixing line between Eastern North Atlantic Water of subtropical origin (ENAW$_{ST}$, S_A = 35.8-36.3 g kg^{-1}, Θ = 12.2-14.8°C; Pollard et al. 1996) and Northeast Atlantic Deep Water (NEADW, S_A = 35.11-35.13 g kg^{-1}, Θ = 2.6-3.0°C; van Aken 2000) towards the canyon head (Fig. 6b). Eastern North Atlantic Water of subpolar origin (ENAW$_{SP}$, S_A = 35.4-35.8 g kg^{-1}, Θ = 8.5-12.2°C; Pollard et al. 1996) and Mediterranean Water (MEDW, $S_A > 35.9$ g kg^{-1}, $\Theta \approx 9.5$°C; Harvey 1982), identified by local salinity minima and maxima, respectively, at VMs 2-4 are almost completely absent at VM5.

Secondly, the gradient of dissolved oxygen concentration through the deep oxycline (250-750 m) weakened towards all three canyon heads in the study region (Fig. 6c). Below the mixed layer and photic zone, $d[\text{O}_2]/dt$ is small on the timescale of the study, so dissolved oxygen can be considered a conservative tracer. A weak gradient indicates a more homogenised watercolumn, possibly a result of elevated levels of turbulent mixing due to internal tide dissipation. Dissolved oxygen concentrations, measured by the Aanderaa optode on the glider, were calibrated against the dissolved oxygen sensor on the ship's CTD rosette. The gradient between 250 m and 750 m, the depth range of the deep oxycline determined from the ship CTD cast (Fig 6d), was calculated by linear least squares regression. The timeseries shows a clear semidiurnal signal from vertical displacement of the oxycline by the internal tide (Fig. 6a), so the gradient was recalculated after first smoothing dissolved oxygen concentration on depth levels using a 25-hour gaussian tapered window running mean ($\sigma = 5$ hours). Gradients varied from consistently >0.13 µmol kg^{-1} m^{-1} around VMs 1, 2, 3a, 4 and 8, to <0.1 µmol kg^{-1} m^{-1} around VM5, near the head of the main canyon limb. Near the other two canyon heads (VM6 and VM7) intermediate gradients were observed, 0.1-0.12 µmol kg^{-1} m^{-1}. For the stations with two occupations (VM3 and VM6), the gradients were smaller during the second occupation (near spring tide) than the first (near neap tide), suggesting modulation of turbulent mixing by the spring-neap cycle.

5. Discussion

Observations of vertical isopycnal displacement at four stations along the main eastern limb of Whittard Canyon show a good fit to a 1-D model of a 25% partly standing internal tide, with the major component

---

[2]Along-canyon distance is defined as positive up-canyon and zero at $H = 1000$ m.
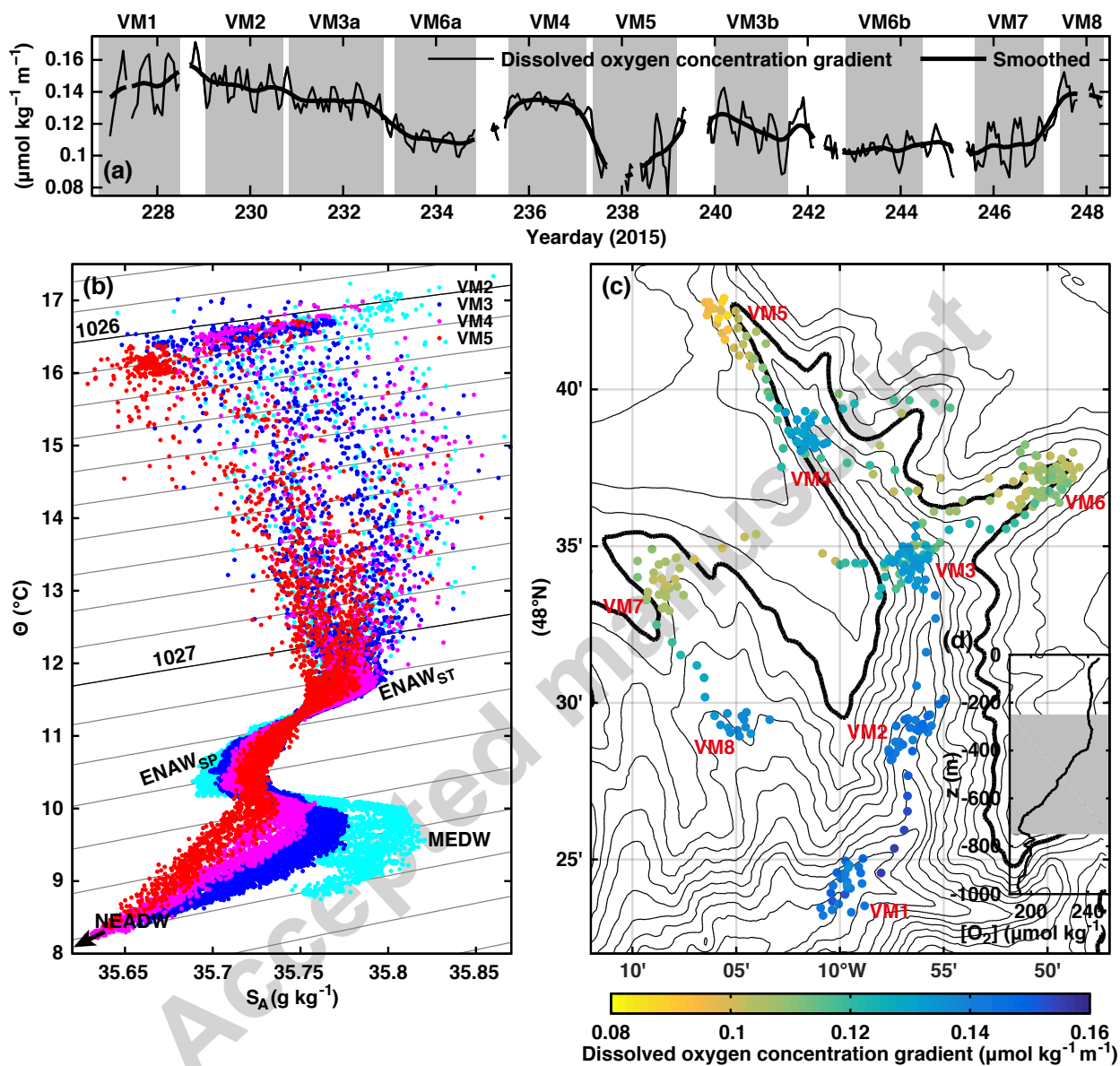
Figure 6: (a) Timeseries of dissolved oxygen concentration gradient through the deep oxycline. The thin line is as observed, the thick line is smoothed using a 25-hour gaussian tapered window running mean. (b) Temperature-salinity plots for four stations along the main canyon limb. (b) Spatial distribution of smoothed dissolved oxygen concentration gradient. (c) Profile of dissolved oxygen concentration from the ship CTD cast showing the deep oxycline between 250 m and 750 m.

12

wave propagating up-canyon. We can use the observation-model derived estimates of along-canyon energy flux (F_x^{obs}) to sketch the propagation of energy through the canyon (Fig. 2c) and further apply the method to VMs 7 and 8 in the adjacent canyon limb. Here too a 25% partly standing internal tide is the best fit to the observations and there is along-canyon energy flux convergence with F_x^{obs} decreasing from 11.5 kW m^{-1} at VM8 to 6.4 kW m^{-1} at VM7. The internal tide dissipation rate between these two stations is 3.6×10^{-7} W kg^{-1}.

5.1. Global context

The internal tide energy fluxes estimated here are comparable to those observed in tidally energetic submarine canyons such as Monterey (up to 5 kW m^{-1}; Kunze et al., 2002; Zhao et al., 2012; Wain et al., 2013), Eel (7.6 kW m^{-1}; Waterhouse et al., 2017) and Gaoping (14 kW m^{-1}; Lee et al., 2009). Similarly, our inferred dissipation rates are within the range of those measured and modelled in other canyon systems. Gregg et al. (2011) summarised turbulent kinetic energy (TKE) dissipation rates in Monterey and Ascension Canyons from microstructure measurements (1-2 $\times 10^{-7}$ W kg^{-1}) and compared them to dissipation rates from regional tide models (4-8 $\times 10^{-8}$ W kg^{-1}). Using Thorpe scale methods, Waterhouse et al. (2017) estimated the tidally- and depth-averaged TKE dissipation rate in Eel Canyon to be 4.2×10^{-8} W kg^{-1}. In the more energetic Goaping Canyon, TKE dissipation rates as high as 4-10 $\times 10^{-6}$ W kg^{-1} have been measured using similar methods (Lee et al., 2009). The latter are an order of magnitude larger than the highest dissipation rates inferred here. Although the observed up-canyon decrease in ENAW$_{SP}$/MEDW and weakening of the dissolved oxygen concentration gradient are indications of enhanced mixing within the canyon, direct turbulent mixing measurements, using a microstructure profiler or a microstructure sensor equipped glider, will be required to fully validate our results.

5.2. Internal spring-neap cycle

The method used here for removing the internal spring-neap cycle relies on the assumption of a local generation site and therefore that the internal spring-neap cycle is phase-locked and proportional to the surface spring-neap cycle. In reality this is unlikely to be strictly true, but the convergence of two independent estimates of $\widetilde{APE}$ at VM3 after the correction was applied suggests the phase-lag between the surface and internal spring-neap cycles is small at this location. Future observational campaigns should aim to fully resolve the internal spring-neap cycle, not only so that it can be effectively removed, but because comparison with the surface spring-neap cycle may provide information on distance to the generation site. To resolve the internal spring-neap cycle using a single glider will require it to occupy a station for two weeks or at minimum return to the same station every 3-4 days. Realistically, these types of observations will require multiple gliders. A multiple-month, multiple-glider observational campaign will also allow the evolution of the internal tide field in response to seasonally changing stratification and mesoscale variability to be determined at high resolution, as well as simultaneous comparison of internal tide dynamics within submarine canyons and over adjacent, smooth continental slopes.

5.3. Internal tide generation sites

The sources of the two component waves that make up the partly standing internal tide cannot be definitively established using the available glider data. However, numerical modelling studies suggest the primary source of the semidiurnal internal tide in the eastern limb of Whittard Canyon is to the southeast, along the Celtic Sea shelf break. A fine-resolution (115-m) nonhydrostatic model simulation of the internal tide field over the Celtic Sea continental shelf and shelf break (Vlasenko et al., 2014) shows packets of internal solitary waves, superposed on semidiurnal internal tides, radiating from several local generators: the shelf break east of the eastern limb of Whittard Canyon; Petite Sole Canyon; and Brenot Spur. Similarly, a high-resolution (500-m) hydrostatic model simulation of the M_2 internal tide in the wider Whittard Canyon region (Aslam, 2017) suggests that Explorer Canyon, Dangeard Canyon and the flanks of Bernot Spur are the primary generation sites for the internal tide in the eastern limb (Fig. 7; Appendix A).

If we assume that the up-canyon, major component wave is generated along the Celtic Sea shelf break or in the lower reaches of the canyon, the down-canyon, minor component wave may either be a reflection
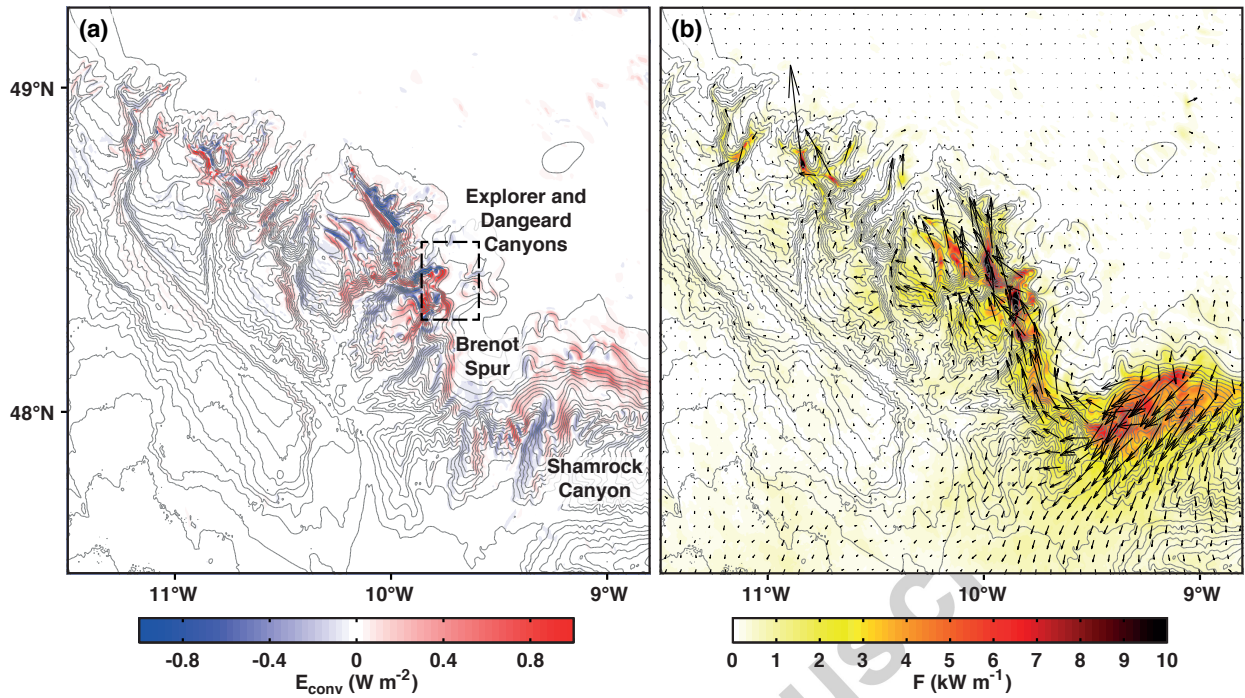
Figure 7: Results from a high-resolution (500-m) hydrostatic model simulation of the M_2 internal tide in the Whittard Canyon region, adapted from Aslam (2017). (a) Barotropic-to-baroclinic energy conversion. Positive values indicate internal tide generation. (b) Depth-integrated internal tide energy flux. Vectors are plotted every 10 grid points (5 km) in each direction. The underlying colour is the energy flux magnitude.
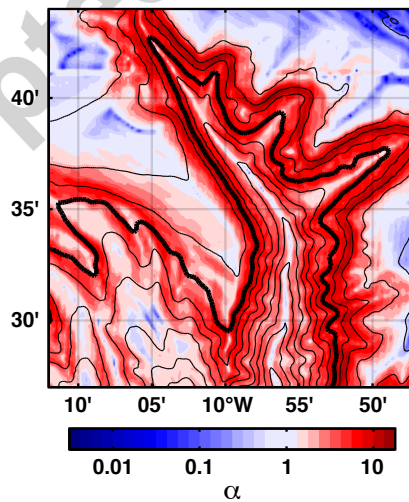

Figure 8: Bathymetric slope criticality to the M_2 internal tide.

of the up-canyon wave or independent internal tide generation near the head of the canyon. The former is likely given the supercritical nature of the steep canyon head bathymetry. Figure 8 shows the distribution of bathymetric slope criticality to the M_2 internal tide,

$$\alpha = \frac{\partial H / \partial \widetilde{x}}{\left[\left(\omega^2 - f^2 \right) / \left(N^2 - \omega^2 \right) \right]^{1/2}}, \tag{9}$$

where $\widetilde{x}$ is across-slope distance and N is taken from the ship CTD cast. Supercritical reflection occurs where $\alpha > 1$ and results in up-slope propagating internal tides being reflected back down-slope. The walls of eastern limb are predominantly supercritical with some sections of upper wall (just beneath the canyon rim) as steep as 1 in 2, a factor of 10 steeper than the M_2 internal tide characteristic at that depth. The canyon floor is typically near-critical ($\alpha \simeq 1$) which suggests that given sufficient forcing an internal bore may develop, as observed at VM6b. Despite the evidence for supercritical reflection, independent internal tide generation cannot be ruled out. In the Whittard Canyon system, internal tide generation is spatially heterogeneous, with adjacent areas of positive and negative barotropic-to-baroclinic energy conversion (Fig. 7a). Spatially integrated over the eastern limb, energy conversion is comparable to energy flux convergence (Aslam, 2017).

5.4. Observational considerations

Whether due to reflection or independent generation, the down-canyon wave has only 6.25% of the total energy density and energy flux of the up-canyon wave; for example the up- and down-canyon energy fluxes at VM5 are 2.12 kW m^{-1} and -0.13 kW m^{-1}, respectively. This implies that misinterpreting a 25% partly standing internal tide as a progressive wave with the amplitude of the major component will overestimate energy dissipation and internal tide driven mixing by 6.25%. For a 50% partly standing internal tide the overestimate is 25%. Calculating energy flux using Equ. 8 avoids such misinterpretations as it is independent of the type of wave. However, inferring energy fluxes from displacement only (or velocity only) observations, combined with theoretical estimates of group speed and HKE/APE ratio, must be done with great care. Perceived group speed for standing or partly standing waves is lower than theoretical group speed, $c_g^{theory} = c_n \sqrt{\omega^2 - f^2}/\omega$ (Gill, 1982), for progressive waves (Alford and Zhao, 2007; Martini et al., 2007; Zhao et al., 2012; Hall et al., 2014). Theoretical HKE/APE ratio, $E_{ratio}^{theory} = (\omega^2 + f^2)/(\omega^2 - f^2)$ (Gill, 1982), only applies to progressive waves; observed E_{ratio} is spatially varying for non-progressive cases, with alternating maxima and minima at one-quarter horizontal wavelength intervals (Nash et al., 2004, 2006; Martini et al., 2007). This is particularly a problem for glider studies as ADCPs are not routinely integrated due to their high power consumption. Unless the (partly) standing nature of a wave is identified, energy fluxes are likely to be overestimated if displacement observations are near **u**-nodes and underestimated if near ξ-nodes.

5.5. Biological impacts

The steep walls of Whittard Canyon, sections of which are vertical or overhanging, provide habitats for a diverse variety of benthic fauna, including cold-water corals, *Lophelia pertusa* and *Solenosmilia variabilis*, limid bivalves, *Acesta excavata*, and deep-water oysters, *Neopycnodonte zibrowii* (Huvenne et al., 2011; Johnson et al., 2013; Robert et al., 2015). These organisms will be directly exposed to the large-amplitude internal tides observed in the canyon. It has been hypothesised that internal tides impact benthic fauna through elevated near-bottom current velocities leading to particle resuspension (Rice et al., 1990), horizontal fluxes of organic material (Frederiksen et al., 1992; White and Dorschel, 2010; Mienis et al., 2007), and the formation of benthic and intermediate nepheloid layers (Mienis et al., 2007; Johnson et al., 2013; Wilson et al., 2015). Although near-bottom current velocity was not directly measured during the study, the 1-D internal tide model predicts near-bottom horizontal velocities, $\mathbf{u}(x, -H, t)$, up to 14 cm s^{-1} for the 25% partly standing wave case, slightly larger than the progressive wave case. These baroclinic velocities are in addition to barotropic tidal currents that are order 10 cm s^{-1} in the region, as measured by the glider using a dive-average current method (Eriksen et al., 2001; Frajka-Williams et al., 2011) and M_2 harmonic analysis. Total (barotropic plus baroclinic) tidal current velocity could therefore be up to 20 cm s^{-1} in
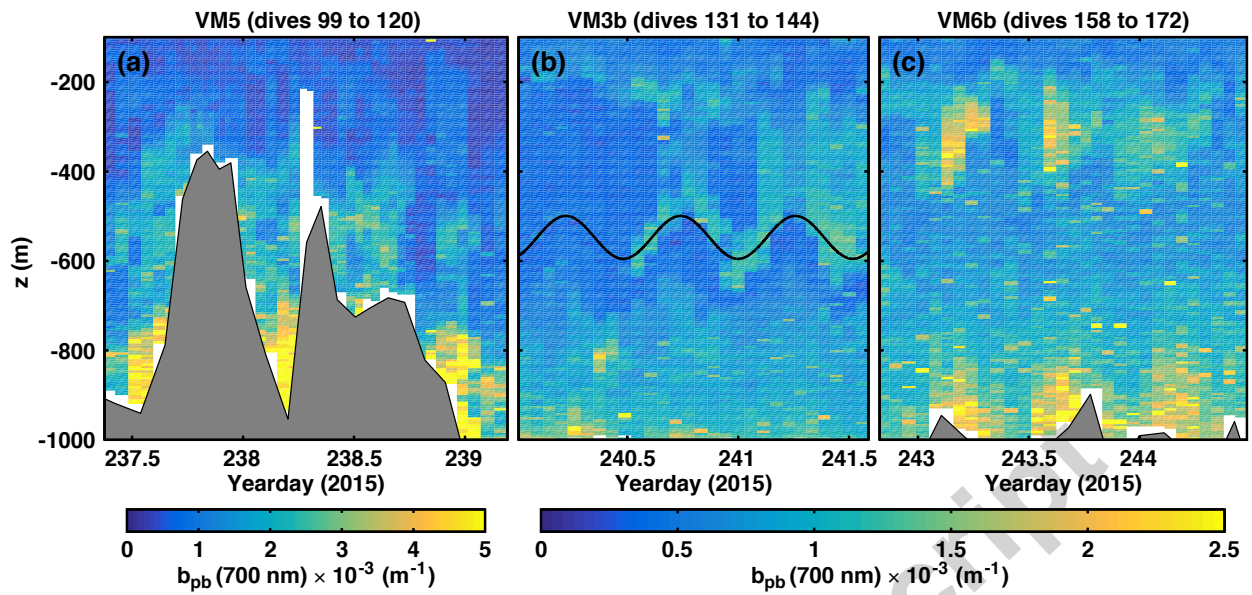
Figure 9: Particulate backscatter at (a) VM5, (b) VM3b, and (c) VM6b. Note the colour scale for panel (a) is twice as broad as for panels (b) and (c). The dotted white line is the glider's path and shows the temporal sampling resolution. The bathymetry (grey) is from soundings using the glider's altimeter. The black line in panel (b) is M_2 harmonically filtered vertical isopycnal displacement at 550 m.
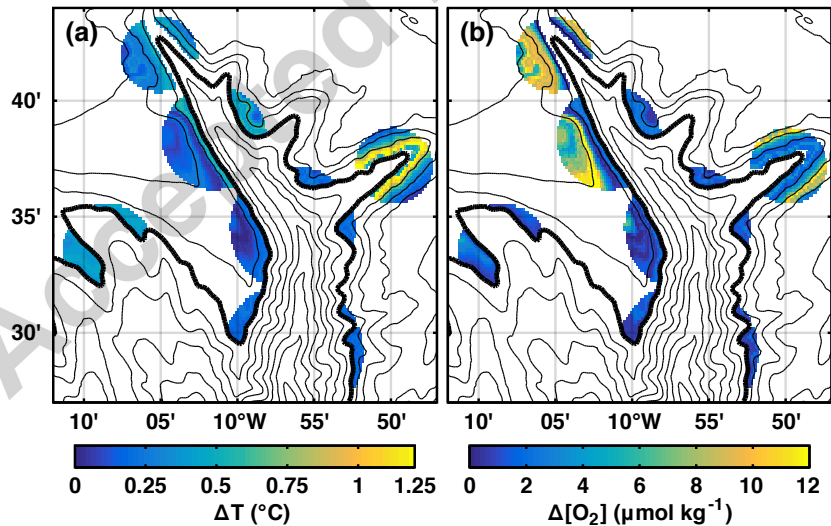

Figure 10: (a) Temperature range and (b) dissolved oxygen concentration range along the canyon walls due to the observed M_2 internal tide.

some areas of the canyon, high enough to cause particle resuspension (Thomsen and Gust, 2000). Elevated near-bottom current velocities are also expected in areas of near-critical bathymetric slope, such as along the canyon floor (Fig. 8), due to trapping of baroclinic energy against the boundary.

Analysis of particulate backscatter (b_{bp}) from the WETLabs sensor on the glider (Appendix B) suggests very high concentrations of suspended particulate matter in the bottom 200 m near the head of the main canyon limb (VM5; Fig. 9a). This is where internal tide current velocities are expected to be high due to topographic focusing of baroclinic energy and could potentially drive particle resuspension. In addition to high particulate backscatter near the canyon floor, possible intermediate nepheloid layers were identified at VM3b (Fig. 9b) and VM6b (Fig. 9c) at around 550 m and 300 m, respectively. These nepheloid layers were only apparent during the second occupation of the stations (near spring tide) suggesting their formation is tidally controlled. The nepheloid layer at VM3b was observed to be vertically displaced ≈100 m by the semidiurnal internal tide while at VM6b the intensity of both benthic and intermediate nepheloid layers appeared to be modulated by the semidiurnal tide.

The effect of tidal hydrodynamics on benthic fauna is the subject of ongoing research. Focusing on cold-water coral mounds on Rockall Bank, van Haren et al. (2014) and Cyr et al. (2016) observed and modelled topographically-trapped diurnal waves and turbulent mixing over the mounds, while Mohn et al. (2014) correlated intensified near-bottom tidal currents to coral occurrence at these and other mounds in the Northeast Atlantic. Within Whittard Canyon, Robert et al. (2015) used predictive habitat models to link the spatial variation in observed biological characteristics (e.g., megafaunal abundance, species richness, and biodiversity) to bathymetry-derived environmental variables (e.g., depth, slope, and roughness), but suggest that the addition of hydrodynamic variables related to internal tides may reduce the amount of unexplained variation. To this end, we estimate the range of temperatures and dissolved oxygen concentrations that organisms on the canyon walls will experience due to vertical displacement of the deep thermocline (beneath 500 m) and oxycline (250-750 m) by the observed M_2 internal tide. At each station and on each depth level ξ_A is compared with the station-mean temperature profile to determine the range of temperatures (ΔT) experienced at that level. This range is projected onto any bathymetry within a defined radius that intersects the depth level and the method repeated for dissolved oxygen concentration. The radius used is $\lambda/20$ (where λ is theoretical M_2 mode-1 horizontal wavelength) which results in no overlapping areas of influence. The greatest temperature variability is around VM6 between 800 m and 1000 m, where ΔT can exceed 1°C (Fig. 10a), and is associated with vertical velocities up to 1.5 cm s^{-1}. This is comparable to diurnal and semidiurnal temperature variability observed at cold-water coral mounds on Rockall Bank (Mienis et al., 2007). The greatest dissolved oxygen concentration variability occurs shallower, along the 600 m isobath, and is 10-12 µmol kg^{-1} near the canyon heads (Fig. 10b). Although of limited spatial coverage, these 2-D maps are a way of representing the internal tide field through environmental variables that directly affect benthic fauna. Future observations and integration of numerical model output could allow these maps to be extended over the whole canyon and so be used for future habitat predictions. Complimentary maps of near-bottom current velocity could be derived from ongoing numerical modelling efforts.

6. Summary

An autonomous ocean glider is used to make the first direct measurements of internal tides within Whittard Canyon. The largest directly observed M_2 isopycnal displacement amplitudes were 80 m, however, after correcting for the spring-neap cycle, amplitudes up to 111 m are estimated. Vertical isopycnal displacement observations at four stations along the main eastern limb fit a 1-D model of a 25% partly standing internal tide – comprised of a major, incident wave propagating up-canyon and a minor wave reflected back down-canyon by steep, supercritical bathymetry near the canyon head (Fig. 11). The model allows estimation of along-canyon energy flux which decreases from 9.2 to 2.0 kW m^{-1} over 28 km and yields a dissipation rate of 1-2.5 × 10^{-7} W kg^{-1}. In the absence of direct turbulent mixing measurements, enhanced mixing within the canyon is inferred from collapsed temperature-salinity curves and weakened dissolved oxygen concentration gradients near the canyon heads.

Finally, potential impact of the observed internal tides on benthic fauna is assessed. Order 20 cm s^{-1} near-bottom current velocities are inferred, possibly resulting in the observed high concentrations of sus-
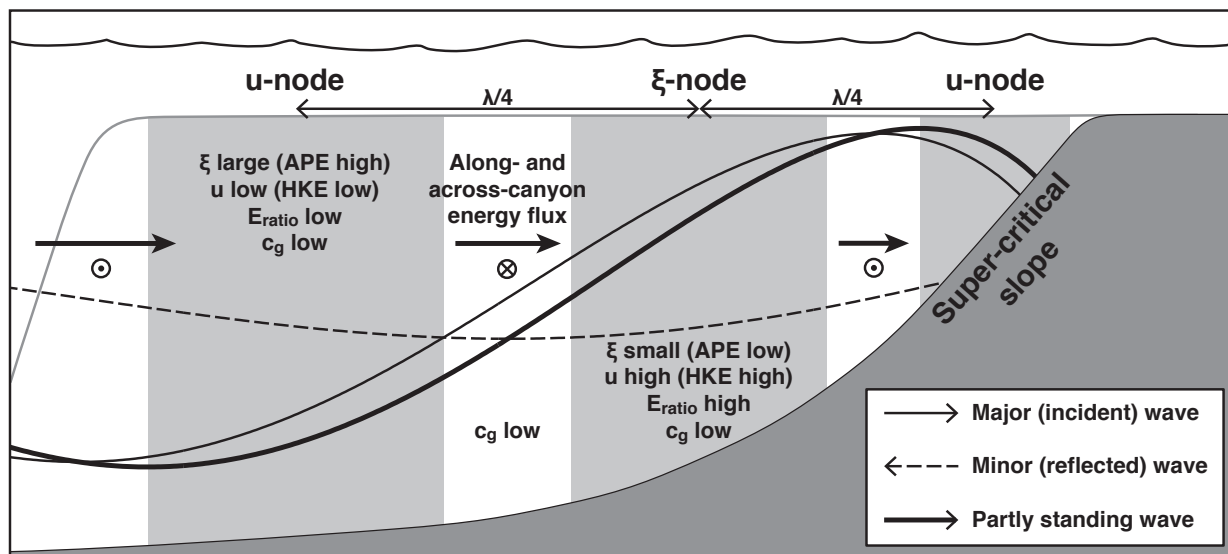
Figure 11: Schematic of a partially standing internal tide in a submarine canyon showing areas near **u**-nodes and ξ-nodes where HKE/APE ratio (E_{ratio}) is low and high, respectively, relative to a progressive internal tide. **u**-nodes and ξ-nodes alternate at one-quarter horizontal wavelength intervals along the canyon. Perceived group velocity (c_g) is low relative to a progressive internal tide at all locations. Along-canyon energy flux is in the direction of the major component wave (up-canyon). Across-canyon energy flux direction alternates between the **u**-nodes and ξ-nodes.

pended particulate matter. The glider observations are also used to estimate a 1°C temperature range and 12 μmol kg^{-1} dissolved oxygen concentration range, experienced twice a day by organisms on the canyon walls, due to vertical displacement of the deep thermocline and oxycline. These large fluctuations in environmental conditions have the potential to greatly affect benthic faunal abundance and distribution so it is essential to consider internal tides and other hydrodynamic processes in the planning of habitat mapping surveys and management of marine protected areas.

Acknowledgments

Appendix A. High-resolution model configuration

A modified version of the Princeton Ocean Model (POM; Blumberg and Mellor, 1987) is used to simulate the M_2 internal tide in the Whittard Canyon region. POM is a three-dimensional, nonlinear, hydrostatic, free-surface, finite-difference, terrain-following (σ coordinate), primitive equation model. The Flather condition (Flather, 1976) is applied at the boundaries so that barotropic energy is transmitted out of the domain. Baroclinic energy is absorbed at the boundaries using the relaxation scheme described by Carter and Merrifield (2007). The model has previously been used to simulate the internal tide field over the Hawaiian Ridge (Carter et al., 2008), Mid-Atlantic Ridge (Zilberman et al., 2009), within Monterey Canyon (Hall and Carter, 2011), and the Faroe-Shetland Channel (Hall et al., 2011).

18

The model domain extends from 12°19.4′W, 46°42.3′N to 8°30.6′W, 49°40.5′N with 500-m horizontal resolution; the bathymetry is derived from the INFOMAR 18 arc-second grid and the General Bathymetric Chart of the Oceans (GEBCO) 2014 30 arc-second grid (http://www.gebco.net). Fifty-one evenly spaced sigma levels are used. Initial conditions are no flow and horizontally uniform stratification; the initial temperature and salinity profiles are taken from a CTD cast at 10°11.9′W, 48°15.9′N on 12 July 2009. The model is forced at the boundaries with M_2 barotropic velocities. Elevations and normal velocities used to calculate the Flather boundary condition are taken from the TPXO7.2 global solution (Egbert and Erofeeva, 2002). The simulation is run for 32 tidal cycles (16.56 days) and M_2 harmonic analyses performed over the last 11 cycles. Baroclinic-to-barotropic energy conversion, $E_{conv} = \langle p'(-H)(-\overline{\mathbf{u}} \cdot \nabla H) \rangle$, where $\overline{\mathbf{u}}$ is depth-averaged velocity (Niwa and Hibiya, 2001), and depth-integrated internal (baroclinic) tide energy flux (Equ. 8) are calculated from the output of the harmonic analyses. Positive energy conversion indicates internal tide generation. Full details of the model configuration and validation against observational datasets are described in Aslam (2017).

Appendix B. Calculation of particulate backscatter

Particulate backscatter was calculated from the 700 nm channel of the WETLabs Eco Puck optical sensor (BB2FLVMT) following Green et al. (2014). The sensor measures the total volume scattering function at a wavelength of 700 nm and a centroid angle of 124° (β(700 nm, 124°); m^{-1} sr^{-1}). The particulate volume scattering function is $\beta_p = \beta - \beta_{sw}$, where β_{sw} is the volume scattering function of pure seawater, dependent on wavelength, scattering angle, temperature and salinity. Following Zhang et al. (2009), β_{sw} at 700 nm, 124°, and for the range of temperatures and salinities that occur in Whittard Canyon, is $5 \pm 0.07 \times 10^{-5}$ m^{-1} sr^{-1} so for simplicity we use a constant value of 5×10^{-5} m^{-1} sr^{-1}. Particulate backscatter in m^{-1} is then calculated $b_{bp}(700 \text{ nm}) = 2\pi \chi_p \beta_p(700 \text{ nm}, 124°)$, where χ_p is the conversion factor between the particulate volume scattering function measured at a fixed angle and particulate backscatter. The conversion factor can be assumed to be wavelength invariant in the absence of phytoplankton blooms (Chami et al., 2006), but is dependent on scattering angle. Following Boss and Pegau (2001) and Chami et al. (2006) we take χ_p to be 1.2 for a scattering angle of 124°. Repeating the method for the 470 nm channel yields qualitatively identical results but an increase in backscatter intensity of $\approx 4 \times 10^{-4}$ m^{-1}.

van Aken, H.M., 2000. The hydrography of the mid-latitude northeast Atlantic Ocean I: The deep water masses. Deep-Sea Research I 47, 757–788.

Alford, M.H., Zhao, Z., 2007. Global patterns of low-mode internal-wave propagation. Part II: Group velocity. Journal of Physical Oceanography 37, 1849–1858.

Allen, S.E., de Madron, X.D., 2009. A review of the role of submarine canyons in deep-ocean exchange with the shelf. Ocean Science 5, 607–620.

Amaro, T., Huvenne, V.A.I., Allcock, A.L., Aslam, T., Davies, J.S., Danovaro, R., De Stigter, H.C., Duineveld, G.C.A., Gambi, C., Gooday, A.J., Gunton, L.M., Hall, R., Howell, K.L., Ingels, J., Kiriakoulakis, K., Kershaw, C.E., Lavaleye, M.S.S., Robert, K., Stewart, H., Van Rooij, D., White, M., Wilson, A.M., 2016. The Whittard Canyon - A case study of submarine canyon processes. Progress in Oceanography 146, 38–57, doi:10.1016/j.pocean.2016.06.003.

Aslam, T., 2017. Internal tides in Whittard Canyon. Ph.D. thesis. School of Environmental Sciences, University of East Anglia.

Blumberg, A.F., Mellor, G.L., 1987. A description of a three-dimensional coastal ocean circulation model, in: Heaps, N.S. (Ed.), Three-Dimensional Coastal Ocean Models, Vol. 4, American Geophysical Union, Washington, DC. pp. 1–16.

Boss, E., Pegau, W.S., 2001. Relationship of light scattering at an angle in the backward direction to the backscattering coefficient. Applied Optics 40, 5503–5507.

Carter, G.S., Gregg, M.C., 2002. Intense, variable mixing near the head of Monterey Submarine Canyon. Journal of Physical Oceanography 32, 3145–3165.

Carter, G.S., Merrifield, M.A., 2007. Open boundary conditions for regional tidal simulations. Ocean Modelling 18, 194–209, doi:10.1016/j.ocemod.2007.04.003.

Carter, G.S., Merrifield, M.A., Becker, J.M., Katsumata, K., Gregg, M.C., Luther, D.S., Levine, M.D., Boyd, T.J., Firing, Y.L., 2008. Energetics of M_2 barotropic-to-baroclinic tidal conversion at the Hawaiian Islands. Journal of Physical Oceanography 38, 2205–2223, doi:10.1175/2008JPO3860.1.

Chami, M., Marken, E., Stamnes, J.J., Khomenko, G., Korotaev, G., 2006. Variability of the relationship between particulate backscattering coefficient and the volume scattering function measured at fixed angles. Journal of Geophysical Research 111, C05013, doi.10.1029/2005JC003230.

Cyr, F., van Haren, H., Mienis, F., Duineveld, G., Bourgault, D., 2016. On the influence of cold-water coral mound size on flow hydrodynamics, and vice versa. Geophysical Research Letters 43, 775–783, doi:10.1002/2015GL067038.

De Leo, F.C., Smith, C.R., Rowden, A.A., Bowden, D.A., Clark, M.R., 2010. Submarine canyons: hotspots of benthic biomass and productivity in the deep sea. Proceedings of the Royal Society B 277, 2783–2792, doi:10.1098/rspb.2010.0462.

Egbert, G.D., Erofeeva, S.Y., 2002. Efficient inverse modeling of barotropic ocean tides. Journal of Atmospheric and Oceanic Technology 19, 183–204.

Egbert, G.D., Erofeeva, S.Y., Ray, R.D., 2010. Assimilation of altimetry data for nonlinear shallow-water tides: Quarter-diurnal tides of the Northwest European Shelf. Continental Shelf Research 30, 668–679, doi:10.1016/j.csr.2009.10.011.

Eriksen, C.C., Osse, T.J., Light, R.D., Wen, T., Lehman, T.W., Sabin, P.J., Ballard, J.W., Chiodi, A.M., 2001. Seaglider: a long-range autonomous underwater vehicle for oceanographic research. IEEE Journal of Oceanic Engineering 26, 424–436, doi:10.1109/48.972073.

Flather, R.A., 1976. A tidal model of the north-west European continental shelf. Memoires de la Societe Royale des Sciences de Liege 6, 141–164.

Frajka-Williams, E., Eriksen, C.C., Rhines, P.B., Harcourt, R.R., 2011. Determining vertical water velocities from Seaglider. Journal of Atmospheric and Oceanic Technology 28, 1641–1656, doi:10.1175/2011JTECHO830.1.

Frederiksen, R., Jensen, A., Westerberg, H., 1992. The distribution of the scleractinian coral *Lophelia pertusa* around the Faroe Islands and the relation to internal tide mixing. Sarsia 77, 157–171.

Garau, B., Ruiz, S., Zhang, W.G., Pascual, A., Heslop, E., Kerfoot, J., Tintoré, J., 2011. Thermal lag correction on Slocum CTD glider data. Journal of Atmospheric and Oceanic Technology 28, 1065–1071, doi:10.1175/JTECH–D–10–05030.1.

García Lafuente, J., Sarhan, T., Vargas, M., Vargas, J., Plaza, F., 1999. Tidal motions and tidally-induced fluxes through La Línea submarine canyon, western Alboran Sea. Journal of Geophysical Research 104, 3109–3119.

Gill, A.E., 1982. Atmosphere-Ocean Dynamics. Academic Press.

Gordon, R.L., Marshall, N.F., 1976. Submarine canyons: internal wave traps? Geophysical Research Letters 3, 622–624.

Green, J.A.M., Simpson, J.H., Legg, S., Palmer, M.R., 2008. Internal waves, baroclinic energy fluxes and mixing at the European shelf edge. Continental Shelf Research 28, 937–950, doi:10.1016/j.csr.2008.01.014.

Green, R.E., Bower, A.S., Lugo-Fernández, A., 2014. First autonomous bio-optical profiling float in the Gulf of Mexico reveals dynamic biogeochemistry in deep waters. PLoS ONE 9, e101658, doi:10.1371/journal.pone.0101658.

Gregg, M.C., Hall, R.A., Carter, G.S., Alford, M.H., Lien, R.C., Winkel, D.P., Wain, D.J., 2011. Flow and mixing in Ascension, a steep, narrow canyon. Journal of Geophysical Research 116, C07016, doi:10.1029/2010JC006610.

Hall, R.A., Alford, M.H., Carter, G.S., Gregg, M.C., Lien, R.C., Wain, D.J., Zhao, Z., 2014. Transition from partly standing to progressive internal tides in Monterey Submarine Canyon. Deep-Sea Research II 104, 164–173, doi:10.1016/j.dsr2.2013.05.039.

Hall, R.A., Carter, G.S., 2011. Internal tides in Monterey Submarine Canyon. Journal of Physical Oceanography 41, 186–204, doi:10.1175/2010JPO4471.1.

Hall, R.A., Huthnance, J.M., Williams, R.G., 2011. Internal tides, nonlinear internal wave trains, and mixing in the Faroe-Shetland Channel. Journal of Geophysical Research 116, C03008, doi:10.1029/2010JC006213.

van Haren, H., Mienis, F., Duineveld, G.C.A., Lavaleye, M.S.S., 2014. High-resolution temperature observations of a trapped nonlinear diurnal tide influencing cold-water corals on the Logachev mounds. Progress in Oceanography 125, 16–25, doi:10.1016/j.pocean.2014.04.021.

Harris, P.T., Whiteway, T., 2011. Global distribution of large submarine canyons: Geomorphic differences between active and passive continental margins. Marine Geology 285, 69–86, doi:10.1016/j.margeo.2011.05.008.

Harvey, J., 1982. θ-S relationships and water masses in the eastern North Atlantic. Deep-Sea Research A 8, 1021–1033.

Hopkins, J.E., Stephenson, G.R., Green, J.A.M., Inall, M.E., Palmer, M.R., 2014. Storms modify baroclinic energy fluxes in a seasonally stratified shelf sea: Inertial-tidal interaction. Journal of Geophysical Research: Oceans 119, 6863–6883, doi:10.1002/2014JC010011.

Hotchkiss, F.S., Wunsch, C., 1982. Internal waves in Hudson Canyon with possible geological implications. Deep-Sea Research 29, 415–442.

Howell, K.L., Davies, J.S., Narayanaswamy, B.E., 2010. Identifying deep-sea megafaunal epibenthic assemblages for use in habitat mapping and marine protected area network design. Journal of the Marine Biological Association of the United Kingdom 90, 33–68, doi:10.1017/S0025315409991299.

Huvenne, V.A.I., Tyler, P.A., Masson, D.G., Fisher, E.H., Hauton, C., Hühnerbach, V., Le Bas, T.P., Wolff, G.A., 2011. A picture on the wall: innovative mapping reveals cold-water coral refuge in submarine canyon. PLoS ONE 6, e28755, doi:10.1371/journal.pone.0028755.

IOC, SCOR, IAPSO, 2010. The international thermodynamic equation of seawater - 2010: Calculation and use of thermodynamics properties, in: Intergovernmental Oceanographic Commission, Manuals and Guides. UNESCO. 56, p. 196.

Johnson, M.P., White, M., Wilson, A., Würzberg, L., Schwabe, E., Folch, H., Allcock, A.L., 2013. A vertical wall dominated by *Acesta excavata* and *Neopycnodonte zibrowii*, part of a undersampled group of deep-sea habitats. PLoS ONE 8, e79917, doi:10.1371/journal.pone.0079917.

Johnston, T.M.S., Rudnick, D.L., 2015. Trapped diurnal internal tides, propagating semidiurnal internal tides, and mixing estimates in the California Current System from sustained glider observations, 2006-2012. Deep-Sea Research II 112, 61–78, doi:10.1016/j.dsr2.2014.03.009.

Johnston, T.M.S., Rudnick, D.L., Kelly, S.M., 2015. Standing internal tides in the Tasman Sea observed by gliders. Journal of Physical Oceanography 45, 2715–2737, doi:10.1175/JPO–D–15–0038.1.

Key, S.A., 1999. Internal tidal bores in the Monterey Canyon. Master's thesis. Naval Postgraduate School. Monterey, CA.

Kiriakoulakis, K., Blackbird, S., Ingels, J., Vanreusel, A., Wolff, G.A., 2011. Organic geochemistry of submarine canyons: The Portuguese Margin. Deep-Sea Research II 58, 2477–2488, doi:10.1016/j.dsr2.2011.04.010.

Kunze, E., MacKay, C., McPhee-Shaw, E.E., Morrice, K., Girton, J.B., Terker, S.R., 2012. Turbulent mixing and exchange with interior waters on sloping boundaries. Journal of Physical Oceanography 42, 910–927, doi:10.1175/JPO–D–11–075.1.

Kunze, E., Rosenfeld, L.K., Carter, G.S., Gregg, M.C., 2002. Internal waves in Monterey Submarine Canyon. Journal of Physical Oceanography 32, 1890–1913.

Lee, I.H., Lien, R.C., Liu, J.T., Chuang, W.S., 2009. Turbulent mixing and internal tides in Gaoping (Kaoping) Submarine Canyon, Taiwan. Journal of Marine Systems 76, 383–396, doi:10.1016/j.jmarsys.2007.08.005.

Lueck, R.G., Osborn, T.R., 1985. Turbulence measurements in a submarine canyon. Continental Shelf Research 4, 681–698.

Martini, K.I., Alford, M.H., Nash, J.D., Kunze, E., Merrifield, M.A., 2007. Diagnosing a partly standing internal wave in Mamala Bay, Oahu. Geophysical Research Letters 34, L17604, doi:10.1029/2007GL029749.

Masson, D.G., Huvenne, V.A.I., de Stigter, H.C., Wolff, G.A., Kiriakoulakis, K., Arzola, R.G., Blackbird, S., 2010. Efficient burial of carbon in a submarine canyon. Geology 38, 831–834, doi:10.1130/G30895.1.

Mienis, F., de Stigter, H.C., White, M., Duineveld, G., de Hass, H., van Weering, T.C.E., 2007. Hydrodynamic controls on cold-water coral growth and carbonate development at the SW and SE Rockall Trough Margin, NE Atlantic Ocean. Deep-Sea Research I 54, 1655–1674, doi:10.1016/j.dsr.2007.05.013.

Mohn, C., Rengstorf, A., White, M., Duineveld, G., Mienis, F., Soetaert, K., Grehan, A., 2014. Linking benthic hydrodynamics and cold-water coral occurrences: A high resolution model study at three cold-water provinces in the NE Atlantic. Progress in Oceanography 122, 92–104, doi:10.1016/j.pocean.2013.12.003.

Nash, J.D., Alford, M.H., Kunze, E., 2005. Estimating internal wave energy fluxes in the ocean. Journal of Atmospheric and Oceanic Technology 22, 1551–1570.

Nash, J.D., Kunze, E., Lee, C.M., Sanford, T.B., 2006. Structure of the baroclinic tide generated at Kaena Ridge, Hawaii. Journal of Physical Oceanography 36, 1123–1135.

Nash, J.D., Kunze, E., Toole, J.M., Schmitt, R.W., 2004. Internal tide reflection and turbulent mixing on the continental slope. Journal of Physical Oceanography 34, 1117–1134.

New, A.L., 1988. Internal tidal mixing in the Bay of Biscay. Deep-Sea Research 35, 691–709.

Niwa, Y., Hibiya, T., 2001. Numerical study of the spatial distribution of the M_2 internal tide in the Pacific Ocean. Journal of Geophysical Research 106, 22441–22449.

Petruncio, E.T., Rosenfeld, L.K., Paduan, J.D., 1998. Observations of the internal tide in Monterey Canyon. Journal of Physical Oceanography 28, 1873–1903.

Pollard, R.T., Griffiths, M.J., Cunningham, S.A., Read, J.F., Pérez, F.F., Ríos, A.F., 1996. Vivaldi 1991 - A study of the formation, circulation and ventilation of Eastern North Atlantic Central Water. Progress in Oceanography 37, 167–192.

Porter, M., Inall, M.E., Hopkins, J.E., Palmer, M.R., Dale, A.C., Aleynik, D., Barth, J.A., Mahaffey, C., Smeed, D., 2016. Glider observations of enhanced deep water upwelling at a shelf break canyon: A mechanism for cross-slope carbon and nutrient exchange. Journal of Geophysical Research: Oceans 121, 7575–7588, doi:10.1002/2016JC012087.

Puig, P., Palanques, A., Martín, J., 2014. Contemporary sediment-transport processes in submarine canyons. Annual Review of Marine Science 6, 53–77, doi:10.1146/annurev−marine−010213−135037.

Queste, B.Y., 2014. Hydrographic observations of oxygen and related physical variables in the North Sea and Western Ross Sea Polynya. Ph.D. thesis. School of Environmental Sciences, University of East Anglia.

Rice, A.L., Thurston, M.H., New, A.L., 1990. Dense aggregations of a hexactinellid sponge, *Pheronema carpenteri*, in the Porcupine Seabight (northeast Atlantic Ocean), and possible causes. Progress in Oceanography 24, 179–196.

Robert, K., Jones, D.O.B., Tyler, P.A., Van Rooij, D., Huvenne, V.A.I., 2015. Finding the hotspots within a biodiversity hotspot: fine-scale biological predictions within a submarine canyon using high-resolution acoustic mapping techniques. Marine Ecology 36, 1256–1276, doi:10.1111/maec.12228.

Rudnick, D., 2016. Ocean research enabled by underwater gliders. Annual Review of Marine Science 8, 19–41, doi:10.1146/annurev−marine−122414−033913.

Sanchez, R., Morandeau, G., Bru, N., Lissardy, M., 2013. A restricted fishing area as a tool for fisheries management: Example of the Capbreton canyon, southern Bay of Biscay. Marine Policy 40, 180–189, doi:10.1016/j.marpol.2013.02.009.

Sharples, J., Moore, C.M., Hickman, A.E., Holligan, P.M., Tweddle, J.F., Palmer, M.R., Simpson, J.H., 2009. Internal tidal mixing as a control on continental margin ecosystems. Geophysical Research Letters 36, L23603, doi:10.1029/2009GL040683.

Shepard, F.P., Marshall, N.F., McLoughlin, P.A., 1974. Internal waves advancing along submarine canyons. Science 183, 195–198.

Thomsen, L., Gust, G., 2000. Sediment erosion thresholds and characteristics of resuspended aggregates on the western European continental margin. Deep-Sea Research 47, 1881–1897.

Vlasenko, V., Stashchuk, N., 2015. Internal tides near the Celtic Sea shelf break: A new look at a well known problem. Deep-Sea Research I 103, 24–36, doi:10.1016/j.dsr.2015.05.003.

Vlasenko, V., Stashchuk, N., Inall, M.E., Hopkins, J.E., 2014. Tidal energy conversion in a global hot spot: On the 3-D dynamics of baroclinic tides at the Celtic Sea shelf break. Journal of Geophysical Research: Oceans 119, 6863–6883, doi:10.1002/2014JC010011.

Vlasenko, V., Stashchuk, N., Inall, M.E., Porter, M., Aleynik, D., 2016. Focusing of baroclinic tidal energy in a canyon. Journal of Geophysical Research: Oceans 121, 2824–2840, doi:10.1002/2015JC011314.

Wain, D.J., Gregg, M.C., Alford, M.H., Lien, R.C., Hall, R.A., Carter, G.S., 2013. Propagation and dissipation of the internal tide in upper Monterey Canyon. Journal of Geophysical Research 118, 4855–4877, doi:10.1002/jgrc.20368.

Waterhouse, A.F., MacKinnon, J.A., Musgrave, R.C., Kelly, S.M., Pickering, A., Nash, J., 2017. Internal tide convergence and mixing in a submarine canyon. Journal of Physical Oceanography 47, 303–322, doi:10.1175/JPO−D−16−0073.1.

White, M., Dorschel, B., 2010. The importance of the permanent thermocline to the cold water carbonate mound distribution in the NE Atlantic. Earth and Planetary Science Letters 296, 395–402, doi:10.1016/j.epsl.2010.05.025.

Wilson, A.M., Raine, R., Mohn, C., White, M., 2015. Nepheloid layer distribution in the Whittard Canyon, NE Atlantic Margin. Marine Geology 367, 130–142, doi:10.1016/j.margeo.2015.06.002.

Zhang, X., Hu, L., He, M.X., 2009. Scattering by pure seawater: Effect of salinity. Optics Express 17, 5698–5710.

Zhao, Z., Alford, M.H., Lien, R.C., Gregg, M.C., Carter, G.S., 2012. Internal tides and mixing in a submarine canyon with time-varying stratification. Journal of Physical Oceanography 42, 2121–2142, doi:10.1175/JPO–D–12–045.1.

Zilberman, N.V., Becker, J.M., Merrifield, M.A., Carter, G.S., 2009. Model estimates of M_2 internal tide generation over Mid-Atlantic Ridge topography. Journal of Physical Oceanography 39, 2635–2651, doi:10.1175/2008JPO4136.1.